ACS APPLIED MATERIALS & INTERFACES

www.acsami.org Research Article

Effect of Selenium Content on Nickel Sulfoselenide-Derived Nickel (Oxy)hydroxide Electrocatalysts for Water Oxidation

Bryan R. Wygant, Anna H. Poterek, James N. Burrow, and C. Buddie Mullins*

Cite This: *ACS Appl. Mater. Interfaces* 2020, 12, 20366–20375 Read Online

ACCESS | Metrics & More | Article Recommendations | Supporting Information

ABSTRACT: An efficient and inexpensive electrocatalyst for the oxygen evolution reaction (OER) must be found in order to improve the viability of hydrogen fuel production *via* water electrolysis. Recent work has indicated that nickel chalcogenide materials show promise as electrocatalysts for this reaction and that their performance can be further enhanced with the generation of ternary, bimetallic chalcogenides (*i.e.*, $Ni_{1-a}M_aX_2$); however, relatively few studies have investigated ternary chalcogenides created through the addition of a second chalcogen (*i.e.*, $NiX_{2-a}Y_a$). To address this, we studied a series of Se-modified Ni_3S_2 composites for use as OER electrocatalysts in alkaline solution. We found that the addition of Se results in the creation of Ni_3S_2/NiSe composites composed of cross-doped metal chalcogenides and show that the addition of 10% Se reduces the overpotential required to reach a current density of 10 mA/cm^2 by 40 mV *versus* a pure nickel sulfide material. Chemical analysis of the composites' surfaces shows a reduction in the amount of nickel oxide species with Se incorporation, which is supported by transmission electron microscopy; this reduction is correlated with a decrease in the OER overpotentials measured for these samples. Together, our results suggest that the incorporation of Se into Ni_3S_2 creates a more conductive material with a less-oxidized surface that is more electrocatalytically active and resistant to further oxidation. Importantly, oxidation does still occur, and the active catalyst is most likely a nickel (oxy)hydroxide surrounding a crystalline, conductive $Ni_3S_{2-x}Se_x$ core.

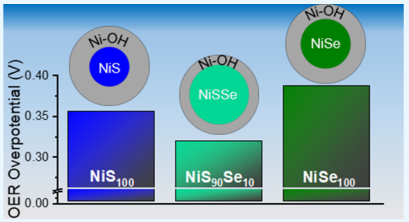

KEYWORDS: *water splitting, oxygen evolution reaction, metal chalcogenide, precatalyst, electrocatalyst, sulfoselenide*

1. INTRODUCTION

As the development and implementation of renewable solar and wind power continues to increase, so too does the need for an efficient means of storing this intermittent energy to allow for efficient incorporation into existing power grids.[1] Much of the recent research on energy storage techniques has focused on technologies such as batteries or chemical fuels, and among the most promising of these is the generation of hydrogen fuel *via* the electrolysis of water.[2] When produced using a clean source of electricity, the only products of the process are H_2 and O_2 gas, which can recombine to produce water and electricity when the fuel is later consumed in a fuel cell or through combustion. Although promising, this technology faces several hurdles to wide-scale implementation, and one of the largest is a need for affordable electrocatalysts to drive the water splitting reactions.

Both halves of the water splitting process require electrocatalysts to reduce the kinetic barriers to electrochemical reaction, but electrocatalysts for the oxygen evolution reaction (OER) are arguably of greater interest, as the OER is the current rate-limiting step for total water electrolysis. The standard benchmark electrocatalysts for the OER are typically costly IrO_2 and RuO_2,[3] and thus, research in the field has been focused on replacing these precious metal catalysts with more earth-abundant materials such as Fe-, Co-, and Ni-based (oxy)hydroxide materials.[4−6] Building on this body of work, a number of promising metal chalcogenide OER catalysts have recently been reported, as well.[5,7−9] In an effort to further improve the catalytic performance of both (oxy)hydroxides and chalcogenides, researchers have modified the compositions of these materials to leverage the synergistic effects of different transition metals, such as Fe and Co, and impact the chemical and electrochemical properties of the catalysts.[6,8,10−12] Recent work has shown that many of these chalcogenide materials may act as precatalysts for the true metal (oxy)hydroxide OER active sites and that the properties of the initial chalcogenide may have a direct impact on the final catalyst that forms.[13,14] As such, researchers have recently begun to systematically incorporate multiple chalcogens into these materials to investigate the resulting effect on OER performance.[15,16] These studies suggest that the incorporation of multiple chalcogens can induce a number of beneficial effects, such as the creation of OER-active crystal lattice defects and improvements in charge conduction, but further work is needed to explore this topic in greater detail.

Received: January 10, 2020
Accepted: April 9, 2020
Published: April 9, 2020

https://dx.doi.org/10.1021/acsami.0c00425
ACS Appl. Mater. Interfaces 2020, 12, 20366–20375

Toward this end, we have used hydrothermal synthesis to create a series of nickel sulfoselenide materials and have investigated their use as OER electrocatalysts. Using a variety of analytical techniques, including X-ray diffraction (XRD), X-ray photoelectron spectroscopy (XPS), scanning and transmission electron microscopy (SEM and TEM), total reflectance X-ray fluorescence spectroscopy (TXRF), electrochemical impedance spectroscopy (EIS), and cyclic voltammetry (CV), we have explored the chemical properties of the materials prior to electrocatalysis to determine what effect the S/Se ratio has on the physical, chemical, and electrocatalytic properties of the materials. We also explored the relative stability of the materials and determined that these nickel sulfoselenides are best classified as precatalysts that yield an active nickel (oxy)hydroxide OER electrocatalyst. Importantly, we find that the incorporation of Se into Ni_3S_2 appears to improve the electrical conductivity and oxidative stability of the metal sulfide and that the degree of surface oxidation prior to the OER correlates well with catalytic performance. Based on our findings, we suggest that metal mixed-chalcogenides such as the nickel sulfoselenides represent a promising family of precatalysts suitable for use in OER electrocatalysis applications. These results open the door for further work in the field of mixed-chalcogenide electrocatalysts for a variety of reactions and the development of advanced catalysts and precatalysts which may improve the affordability of industrial-scale, renewably powered water splitting.

2. EXPERIMENTAL SECTION

2.1. NiS_xSe_y Electrocatalyst Synthesis. All of the NiS_xSe_y electrocatalysts were synthesized using the hydrothermal synthesis detailed here. $Ni(SO)_4{\cdot}6H_2O$ (Acros Organics, 99%, 0.5 mmol) was added to 50 mL of ultrapure water (18 MΩ) and magnetically stirred for 10 min, at which point 5 mmol of the chalcogen precursor was added and the resulting solution was stirred for a further 10 min. Here, thiourea (Acros Organics, 99.9%) was used as the S source, and SeO_2 (Alfa Aesar, 99%) was used as a Se source; in all but the pure NiS_{100}, the total molar chalcogen content was equivalent to the Ni content, and by changing the thiourea/SeO_2 ratio, we controlled the S/Se ratio of the final product. Thus, for a 25% Se-NiS_xSe_y sample, 0.5 mmol of Ni sulfate was combined with 0.375 mmol of thiourea and 0.125 mmol of selenium oxide. In the case of the pure Ni_3S_2, a 3:2 ratio of Ni sulfate/thiourea was used as a 1:1 ratio produced an uneven mix of Ni_3S_2 and NiS_2, rather than NiS.

After mixing of the chalcogen precursors was completed, 10 mL (55× molar equivalents) of hydrazine hydrate solution (Millipore-Sigma, 99%) was added dropwise to the solution over approximately 5 min, and the resulting solution was stirred for an additional 10 min. In the hydrothermal synthesis, the hydrazine acts as a thermally activated reducing agent to produce H_2S and H_2Se, which can in turn produce the Ni chalcogenides. After mixing, the resulting solution was transferred to a Teflon hydrothermal reactor vessel (100 mL) and sealed in a hydrothermal autoclave. The vessel was heated in a muffle furnace at 5 °C/min to 180 °C and held for 20 h before being allowed to cool to room temperature naturally, typically about 6 h. Following cooling, the resulting metal chalcogenide powder was washed in water and centrifuged twice, followed by one more wash in ethanol to remove any unreacted precursors and then dried in a vacuum oven overnight at 80 °C. These dried powders were then collected and used as-synthesized in further characterizations. Of note, this synthesis was relatively robust and showed similar products, crystallography, and morphology, when scaled up to three times the Ni/chalcogen concentration while maintaining the total water and hydrazine hydrate volume.

2.2. Electrocatalyst Ink and Electrode Preparation. In a typical electrode fabrication, 0.5 mg of catalyst powder was suspended in 0.125 mL (4:1 g/mL) of a 4% Nafion (Millipore-Sigma)/isopropanol solution by sonication for 10 min. Following suspension, 12 μL of ink was deposited onto a 0.2 cm^2 glassy carbon rotating disk electrode (RDE, Gamry) in 3 μL aliquots, each followed by drying, to produce a total loading of 0.24 mg/cm^2. Once dried, the electrode was used for electrochemical testing.

2.3. Electrochemical Testing. To determine the overall electrocatalyst performance, we performed CV in approximately 40 mL of 1 M KOH solution (Fisher, ACS Certified) using a CHI 660D potentiostat (CH Instruments, Austin, TX). The NiS_xSe_y/glassy carbon RDE was used as the working electrode, a Pt wire was used as the counter electrode, and an Ag/AgCl reference electrode in saturated KCl solution (CH Instruments, Austin, TX) was used as the reference. In a typical experiment, three consecutive CV sweeps were made from 0.2 to 0.8 V *versus* Ag/AgCl (sat. KCl) with 100% iR compensation at a scan rate of 20 mV/s. For each material, testing was performed in triplicate fashion; three separate electrodes were prepared, and 3 CVs were run on each prepared electrode. The third scan of all three of the electrodes was then employed to generate an average curve from which the overpotential at 10 mA/cm^2 (η_{10}) was measured. EIS was performed on selected NiS_xSe_y samples at an alternating potential of 1.52 V *versus* RHE with an amplitude of ±5 mV between 100 kHz and 0.1 Hz. After the initial EIS spectra were measured, all samples underwent chronopotentiometric testing at 10 mA/cm^2 for 10 min, and the EIS spectra were measured again. For long-term testing of the electrodes, chronopotentiometric experiments were performed by measuring the potential required to produce 10 mA/cm^2 of current as a function of time; the potential was later corrected using the measured resistance of the electrode prior to testing. During long-term testing, the RDE was rotated at approximately 300 rpm and a slow stream of Ar gas was impinged on the surface to dislodge any O_2 bubbles generated during the experiment.

For rotating ring-disk electrode (RRDE) analysis of Faradaic efficiency, a glassy carbon disk electrode loaded with 0.24 mg/cm^2 of the NiS_xSe_y catalyst was used as the working electrode and a Pt ring electrode was used to reduce the O_2 generated at the disk to H_2O_2 *via* a two-electron process; a Ag/AgCl (sat'd KCl) reference electrode and Pt wire counter electrode completed the electrochemical cell, and a CHI 700E bipotentiostat (CH Instruments, Austin, TX) was used to perform the analysis. An Ar-sparged 0.1 M KOH solution was used as the electrolyte for all experiments. All of the experiments were background-corrected by measuring the ring current at 0.435 V *versus* RHE and holding the disk at the open-circuit potential over 2 min while rotating at 1600 rpm; the average ring current of the last 60 s of the experiment was then subtracted from the subsequent ring current measurements. For Faradaic efficiency measurements, the NiS_xSe_y electrocatalyst was held at 1, 2, and 4 mA/cm^2 for 2 min with a rotation rate of 1600 rpm, while the ring was held at 0.435 V *versus* RHE. The average ring and disk currents from the last 60 s of the measurement were used to solve for eq 1, where ε is the Faradaic efficiency, i_r is the ring current, i_d is the disk current, and N is the collection efficiency of the ring (measured as 0.39 in this system). Tests for each electrocatalyst were performed in triplicate, and the average values were reported.

$$\varepsilon = \frac{2i_r}{Ni_d} \tag{1}$$

2.4. Physical Characterization. Powder XRD was performed using a Spider (Rigaku) diffractometer with a Cu Kα radiation source. SEM images were collected using an FEI Quanta 650 environmental scanning electron microscope using a 20 kV accelerating voltage. XPS analysis was performed using a Kratos Axis Ultra photoelectron spectrometer using a monochromated Al Kα excitation source with spectra corrected to the adventitious C 1s peak at 284.8 eV. High-resolution transmission electron microscopy (HRTEM) and energy-dispersive X-ray spectroscopy (EDX) mapping using scanning transmission electron microscopy were all performed on a JEOL 2010F transmission electron microscope with an ultrahigh resolution

https://dx.doi.org/10.1021/acsami.0c00425
ACS Appl. Mater. Interfaces 2020, 12, 20366−20375

pole piece. The EDX mapping was conducted using an Oxford X-MaxN 80TLE solid-state detector. Brunauer–Emmett–Teller (BET) surface area measurements were made using Kr adsorption in a bath of liquid nitrogen at 77 K with a Quantachrome AutoSorb iQ volumetric gas adsorption analyzer (Anton Paar). Because of the low amount of metal chalcogenides produced during our synthesis and the inherently low surface area of the materials (<50 m^2/g), Kr was used as the adsorbate gas for all catalysts. All samples were degassed at 120 °C under vacuum prior to weighing to remove surface-adsorbed species. Multipoint BET analysis was performed using Anton Paar's ASiQ_Win software with a specified P_0 value of 2.63 Torr. ASiQ_Win's "Micropore BET Assistant" was employed for optimal point selection for fitting to the BET equation to determine Kr-accessible surface areas. TXRF quantification of dissolved S, Se, and Ni in electrolyte solution was measured using a S2 Picofox spectrometer (Bruker Nano GmbH) with a Mo K excitation source. The electrolyte solution (0.995 mL) was mixed with 5.0 μL of a Y solution (TraceCERT, 1000 mg/L in nitric acid, Sigma-Aldrich) to act as an internal standard. The resulting solution (10 μL) was dropped onto a quartz disk and dried at 70 °C for 15 min, and the TXRF spectra were acquired over 300 s; three replicates were performed for each NiS_xSe_y catalyst studied. External calibration for quantification was performed using a commercial standard (TraceCERT Periodic Mix Table 1, Sigma-Aldrich). The background concentrations of each analyte in a sample of the KOH electrolyte prior to testing were also measured, and the quantities measured in the tested samples were background-corrected to these values.

Table 1. Gravimetric Overpotential, BET-Derived Overpotential, and BET Surface Areas of NiS_xSe_y Composites

sample	η_{10}, gravimetric (V)	$\eta_{0.5}$, BET SA (V)	SA_{BET} (m^2/g)
NiS_{100}	0.354	0.400	14.6
$NiS_{90}Se_{10}$	0.318	0.368	17.3
$NiS_{75}Se_{25}$	0.324	0.341	10.6
$NiS_{50}Se_{50}$	0.412	0.462	12.7
$NiSe_{100}$	0.386	0.377	5.67

3. RESULTS AND DISCUSSION

3.1. XRD Spectroscopy and SEM. To determine what effect chalcogen substitution has on the hydrothermal synthesis of our nickel sulfoselenide electrocatalysts, we used powder XRD to analyze differences in the crystal structures of a series of materials, ranging from pure nickel sulfide and nickel selenide compounds to a range of S/Se ratios. For simplicity, the composites will be named according to the standard formula NiS_xSe_y, where "x" equals the percentage of S relative to Ni and "y" represents the percentage of Se. Therefore, a composite with 90% S and 10% Se would be referred to as $NiS_{90}Se_{10}$. The results, presented in Figure 1, show that these materials undergo a variety of changes as the S/Se ratio decreases from 9:1 to 1:1. By XRD, the Se-free material, NiS_{100}, is composed of a primary Ni_3S_2 phase and a minor NiS impurity phase, and both phases have been shown to be effective electrocatalysts with comparable OER overpotentials in previous studies.[17−20] With the incorporation of 10% Se, we observe the formation of a discrete NiSe peak near 33° two theta, indicating that the Ni_3S_2 does not accommodate all of the Se in the crystal lattice, resulting in the formation of a Ni_3S_2/NiSe composite. At 25% Se incorporation, the Ni_3S_2 and NiSe phases become equally intense, and by 50% Se incorporation, the Ni_3S_2 becomes the impurity phase in a primarily NiSe composite. As a comparison to the Se-incorporated Ni_3S_2 composites, we also report a pure $NiSe_{100}$ sample, which is composed primarily of NiSe, with a small Ni_3Se_2 impurity.

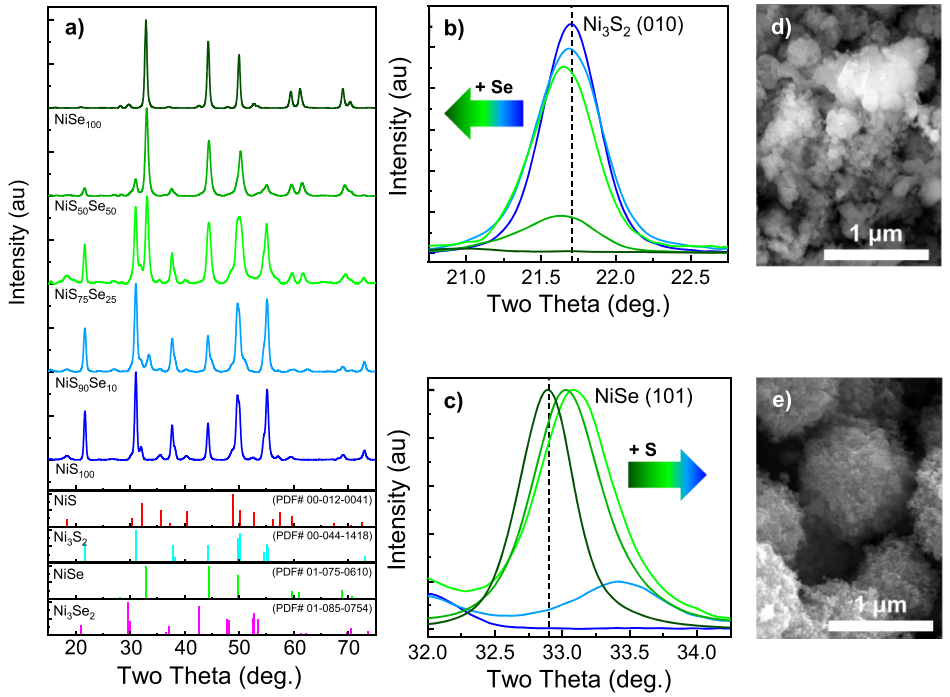

Figure 1. (a) XRD spectra of a series of nickel sulfoselenide composite materials. The primary Ni_3S_2 phase is gradually replaced by NiSe as more Se is added to the composite. (b) Ni_3S_2 (010) peak shows a gradual shift to lower two theta with increasing Se content as more Se is incorporated into the lattice; (c) a similar effect occurs in the NiSe (101) peak, where increasing S-content causes a shift to higher two theta. SEM images of the NiS_{100} (d) and $NiSe_{100}$ (e) show that both composites consist of agglomerated particles between 0.5 and 1 μm in diameter.

https://dx.doi.org/10.1021/acsami.0c00425
ACS Appl. Mater. Interfaces 2020, 12, 20366−20375

The formation of the NiSe impurity at a S/Se ratio of 9:1 indicates that much of the Se is likely segregated into a distinct NiSe phase during synthesis and suggests that the incorporation of the much larger Se anion into the Ni_3S_2 lattice is not favorable.[21] Despite this, the XRD spectra show that some of the Se does become incorporated into the Ni_3S_2 phase. As seen in Figure 1b, there is a slight shift in the position of the Ni_3S_2 (010) peak at 21.7° to smaller two theta with increasing Se concentration, indicative of the incorporation of the larger anion into the crystal lattice. Likewise, a small quantity of S becomes incorporated into the selenide phase, and the $NiSe_{100}$ (101) peak at 32.9° (Figure 1c) exhibits a relatively large half degree shift to larger two theta as the composition becomes more S rich.[15] The magnitude of this shift, as well as the prominence of the NiSe product over Ni_3S_2 at low S/Se ratios, indicates that the smaller S^{2-} anion may be relatively easy to incorporate into the NiSe lattice, although the extent of that substitution is not further studied here.

The XRD spectra reveal that the final product of the hydrothermal synthesis is a Se-doped Ni_3S_2 and S-doped NiSe composite material, where the relative quantity of each component depends on the S/Se ratio. Previous studies of pure nickel sulfide and nickel selenide electrocatalysts have shown that both have good OER performance, with similar overpotentials when tested on high-surface area Ni foam electrodes.[17,22] Importantly, however, the electrocatalysts presented in these two studies had dramatically different morphologies; the NiSe exhibited a nanowire morphology, while the Ni_3S_2 exhibited nanosheet morphology. Because significant differences in morphology and size can impact the comparison of electrocatalytic performance,[14] we used SEM to study the morphology of our mixed NiS_xSe_y samples more closely and ensure that our synthetic procedure produced comparable products. As can be seen in Figure 1d,e, the materials are all composed primarily of roughly spherical particles, with diameters ranging from approximately 500 nm for the NiS_{100} material to approximately 1 μm for the $NiSe_{100}$. Generally, it appears that the Ni_3S_2-rich composites exhibit smaller particles than the NiSe-rich composites, but in all cases, the particles appear to exhibit a degree of surface roughness (Figures S1 and S2). The effect of any apparent roughness on the overall catalyst surface area is small, however, as the BET surface areas of the composites measured using Kr adsorption measurements are all below 20 m^2/g (Figure S3). After comparing the SEM images, BET surface area measurements, and XRD spectra for all of the composites, we note a slight relationship between chalcogenide composition, morphology, and surface area. Low Se concentration (0 and 10% Se) leads to smaller Ni_3S_2 particles with larger surface areas, while increased Se content (50 and 100% Se) appears to induce a transformation to the larger NiSe microspheres visible in SEM, as shown in Figure S2d,e. As evidenced by the XRD spectrum in Figure 1, $NiS_{75}Se_{25}$ appears to represent a transition between these two products, possessing both Ni_3S_2 and NiSe phases in abundance but generally possessing a more Ni_3S_2-like morphology; this combination appears to result in a material which breaks the trend in the relationship between BET surface area and Se content. SEM images in Figures S1c and S2c show that the small Ni_3S_2-like particles present in the $NiS_{75}Se_{25}$ sample agglomerate more than the other composites, while there are also more micrometer-scale spherical NiSe particles visible as well. Together, both features may help to explain the anomalously low BET surface area of the $NiS_{75}Se_{25}$ sample.

3.2. Electrochemical Characterization. Next, we used CV to investigate the effects of these aforementioned differences in physiochemical properties on performance of the composites for the OER in alkaline solution. Using Nafion as a binder, we loaded the catalysts at 0.24 mg/cm^2 on a glassy carbon electrode for testing in a 1 M KOH solution. As seen in Figure 2a, OER performance improves as Se is incorporated into the Ni_3S_2 composite. The overpotentials at 10 mA/cm^2 (η_{10}) of both the $NiS_{90}Se_{10}$ and $NiS_{75}Se_{25}$ samples are approximately 40 mV lower than those of the Se-free NiS_{100} sample. However, further increasing the amount of Se to a 1:1 S/Se ratio results in an increase in overpotential to 412 mV, larger even than that of the pure $NiSe_{100}$ (η_{10} = 386 mV). A similar trend is likewise observed in measurements of mass activity for the catalysts at 300 and 400 mV of overpotential (Figure S4), where the $NiS_{90}Se_{10}$ and $NiS_{75}Se_{25}$ samples showed notably better performance than the other composites tested. The measured η_{10} for all composites suggest that while pure Ni_3S_2 is a better catalyst for the OER than NiSe, the addition of moderate amounts of Se produces doped $Ni_3S_{2-y}Se_y$ catalysts with notably improved OER performance and stability, indicated by the low η_{10} and the minimal change in overpotential over time in Figure 2b.

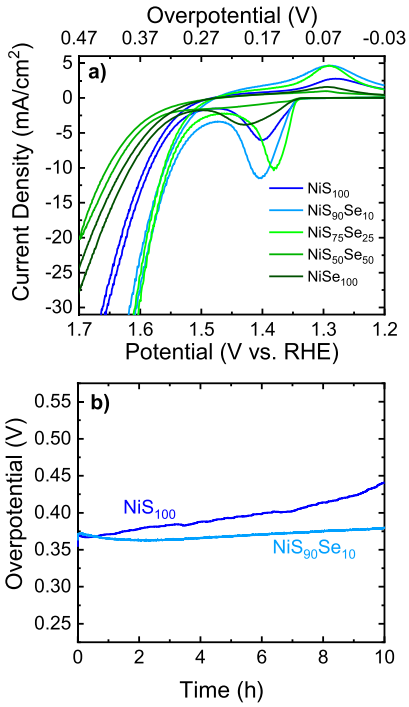

Figure 2. (a) Averaged CVs of the NiSSe composites measured in 1 M KOH. The addition of 10–25% Se significantly reduces the overpotential when compared to the pure sulfide or selenide, as well as the 50/50 mixture. (b) Chronoamperomogram of the NiS_{100} and $NiS_{90}Se_{10}$ composites at 10 mA/cm^2 over 10 h of continuous use, showing the superior stability of the Se-incorporated material. All experiments were performed *vs* a Pt counter electrode with a Ag/AgCl (sat'd KCl) reference electrode.

The increase in overpotential with testing time for the NiS_{100} sample may be due in part to oxidation of the metal chalcogenide surfaces with OER electrocatalysis. Previous studies have shown that metal chalcogenides tend to exhibit

https://dx.doi.org/10.1021/acsami.0c00425
ACS Appl. Mater. Interfaces 2020, 12, 20366–20375

oxidation under OER reaction conditions and that the factors that govern the extent of oxidation for different materials are relatively poorly understood at present.[14] To explore if self-oxidative side reactions may occur at the catalyst surface during the OER, we used a RRDE to calculate the Faradaic efficiency of the NiS_{100}, $NiS_{90}Se_{10}$, and $NiSe_{100}$ composites.[23] Figure S5 shows that over a range of applied j, the $NiS_{90}Se_{10}$ and $NiSe_{100}$ electrocatalysts showed higher Faradaic efficiency than the NiS_{100} sample, which indicates that the presence of Se reduces Faradaic side reactions during the OER. We note that errors on the order of ±10% are not uncommon with this technique,[23] and we believe that the greater than 100% efficiency observed for $NiSe_{100}$ at higher applied current densities (106% at 4 mA/cm^2) is likely due to a systematic error present in our testing apparatus. As such a systematic error is expected to be present in measurements for all three composites, we can make qualitative, if not quantitative, comparisons of the composites' Faradaic efficiencies. TXRF analysis of the electrolytes used to test these composites for 6 h at 10 mA/cm^2 appears to support these results as well. Analysis of three representative samples (NiS_{100}, $NiS_{90}Se_{10}$, and $NiSe_{100}$) showed less dissolved Ni in solution for the Se-containing electrocatalysts after testing (Figure S6) than for the pure sulfide; as Ni is expected to be the binding site for OER catalysis, this helps explain the stability of our $NiS_{90}Se_{10}$ electrocatalyst. Sulfur was not observed in any samples, possibly because of *in situ* reduction at the counter electrode or to other systematic losses, and Se was observed in all samples, likely because of a small degree of surface contamination from the hydrothermal synthesis. We note that the significant quantity of Se detected in the electrolyte after testing the $NiSe_{100}$ sample may suggest chemical etching by KOH rather than electrochemical oxidative degradation, given the high measured Faradaic efficiency of $NiSe_{100}$. Regardless, the decrease in concentration of Ni in the electrolyte with increased Se content indicates that the addition of even small amounts of Se to the NiS_xSe_y composite can increase (electro)chemical stability, as previously observed when comparing the long-term testing in Figure 2b.

Notably, the addition of large amounts of S to a NiSe electrocatalyst actually decreased OER performance relative to a S-free material, despite the increased stability of Se-containing electrocatalysts at low Se concentrations. This result is significant because previous work on materials with a nominal NiSe crystal structure doped with S showed increased performance as the S/Se ratio decreased.[15] Another study on a Se-doped NiS_2 material for the OER in the neutral electrolyte showed that a 1:1 S/Se ratio was optimal, in marked contrast to the relatively poor performance of our $NiS_{50}Se_{50}$ sample.[24] Given that the materials in these previous studies were primarily NiSe and NiS_2, while the predominant crystal structure in our most efficient composites is Ni_3S_2, it appears that the effects of S or Se doping may differ noticeably between metal chalcogenides with different crystal structures. These differences may be due in part to the ease of defect formation in a given crystal structure upon heteroanion incorporation. Wang *et al.* previously showed that NiCoSe nanocrystals doped with S possessed more lattice defects than undoped nanocrystals, which acted as nucleation sites for the formation of the active $NiCo(OH)_2$ phase during catalysis.[15] We postulate that the Se incorporation evidenced in the XRD spectra may likewise induce defects in the Ni_3S_2 lattice and may similarly help to form an active (oxy)hydroxide OER catalyst species. At moderate Se levels of 10 and 25%, Se incorporation appears to improve the performance of predominantly Ni_3S_2 materials. However, above this observed threshold, increasing the Se ratio results instead in the formation of NiSe as the dominant crystalline product with residual S acting as the dopant. Although NiSe-phase nanocrystals of a material with the same S/Se ratio were shown to be efficient for the OER,[15] we observe that the production of defects might not have as significant of an effect in our micron-sized particles.

To more closely probe the fundamental differences in the intrinsic OER performance of these materials, we calculated the BET-derived current density (mA/cm$_{BET}^2$) by dividing the observed current densities (mA/cm$_{RDE}^2$) by the 0.24 mg/cm$_{RDE}^2$ loading and each electrocatalyst's BET specific surface area (SA_{BET}, cm^2/g) as determined by Kr adsorption (Figure S5). These renormalized performance curves are shown in Figure S6, and both the gravimetric and BET-derived results are summarized in Table 1. After accounting for differences in SA_{BET}, the $NiS_{50}Se_{50}$ sample still shows the worst OER performance of all of the composites, while in contrast to the analysis based on the RDE surface area, the $NiS_{75}Se_{25}$ catalyst shows higher geometric activity than the $NiS_{90}Se_{10}$ composite; this is in agreement with previous reports on low S/Se materials[15] and the mass activity measurements of the composites at higher overpotentials (Figure S4). Furthermore, the pure $NiSe_{100}$ material shows a lower SA_{BET}-scaled overpotential than the pure NiS_{100} material, as previously observed by Nath and co-workers.[7] Thus, our composites appear to show that although the intrinsic performance of Se-rich nickel chalcogenides is superior to a point, the gravimetric performance of such composites is inhibited by their lower surface areas, which is likely caused by the formation of larger NiSe microspheres.

Several factors may explain the improved intrinsic activity observed in the Se-containing composites. As previously mentioned, it may be due in part to the presence of lattice defects in the Ni_3S_2 material induced by the substitution of Se for S, as evidenced in Figure 1b. Alternatively, metal selenides are known to be more electronically conductive than metal sulfides, and thus, the inclusion of Se may improve the conductivity of the resulting composite. Higher electrical conductivity and faster electron transfer within the catalyst might reduce resistive losses and improve catalyst performance. To determine if differences in electrical conductivity may be playing a role in the performance difference, we studied the EIS spectra of characteristic NiS_xSe_y electrocatalysts and related this to the previously measured OER performance. Nyquist plots of the catalysts in Figure S8 show that the pristine, untested NiS_{100} electrocatalyst has a significantly larger semicircle than either the $NiS_{90}Se_{10}$ or $NiSe_{100}$ materials. This indicates that the inclusion of just 10% Se into the Ni_3S_2 material significantly improved the conductivity of the material, making it greater even than that of a pure nickel selenide and likely contributing to the enhanced electrocatalytic performance observed in Figure 2a. Because subsequent surface oxidation may decrease electrocatalyst conductivity and impact measured performance, we also recorded the EIS spectra of the samples after 10 min of testing at 10 mA/cm^2. For all materials, the semicircles in the Nyquist plots increased in diameter after testing (Figure S8), an indication of reduced conductivity that can be attributed to the surface oxidation suggested by the measurements of Faradaic efficiency. Among the three samples, $NiS_{90}Se_{10}$

https://dx.doi.org/10.1021/acsami.0c00425
ACS Appl. Mater. Interfaces 2020, 12, 20366−20375

showed a much smaller loss of conductivity than either the NiS_{100} or $NiSe_{100}$, in good agreement with the low η_{10} and high stability of the material. In contrast, both the pure sulfide and selenide materials show much larger semicircles that are indicative of lower conductivities. The $NiSe_{100}$ in particular shows a very large decrease in conductivity after testing, which ultimately results in poorer conductivity than the NiS_{100} sample; this agrees well with the relatively poor electrocatalytic performance previously demonstrated. In addition to the lower surface area of the catalyst, this evidence of decreased conductivity may explain its relatively low performance when compared to pure sulfur and 10% Se materials. Together, our EIS results suggest that conductivity, in addition to the catalyst surface area, plays a significant role in OER electrocatalysis and that the inclusion of small quantities of Se into Ni_3S_2 significantly improves the conductivity of the resulting material.

3.3. X-ray Photoelectron Spectroscopy. We next analyzed the chemical composition of the as-synthesized materials with XPS and EDX to more fully explore the improved performance of the NiS_xSe_y electrocatalysts. Using XPS deconvolution and EDX quantification, we calculated the S/Se ratios of our catalysts (Figure S9a) and found that the relative amount of each chalcogen agrees well with the theoretical values for the desired compositions. However, the $NiS_{90}Se_{10}$ (S/Se theo. = 9.0) material shows a relatively low S/Se ratio of approximately 5.3 from XPS, and this may be due to surface oxidation of the materials following synthesis. Such surface oxidation is supported by the much higher S/Se value of 7.5 obtained *via* EDX (which has a much larger probe depth and is not as sensitive to surface oxidation). Indeed, closer analysis of the O 1s spectra for all materials (Figure S9b) shows a significant hydroxide peak near 531 eV, which likewise indicates that the surface has oxidized even before testing. Notably, as the S/Se ratio decreases, so does the quantity of the oxidized material at the composite surface, as can be seen in both the chalcogen (S 2s/Se 3s) and oxygen (O 1s) spectra for the NiS_{100}, $NiS_{90}Se_{10}$, and $NiSe_{100}$ materials in Figure 3b,c and for all other samples in Figure S9b,c. In all cases, the S 2s and Se 3s spectra contain both a primary metal sulfide/selenide peak (226.2 eV for S and 228.9 eV for Se) and an accompanying oxidized S or Se peak approximately 3−3.5 eV higher. All Se-containing composites show less oxidation than the pure NiS_{100} sample, and within the Se-containing samples, $NiS_{90}Se_{10}$ and $NiS_{75}Se_{25}$ show the smallest quantity of the oxidized material (Figure S9d). Similarly, as the S/Se ratio decreases, the Ni/Ni-X peak in the Ni 2p 3/2 spectra becomes more pronounced and shifts from 853.1 eV for NiS_{100} to a value of approximately 852.3 eV for $NiSe_{100}$ (Figure 3a), as indicated by the dashed line. Combined analysis of these spectra suggests the presence of a more metallic and less-oxidized surface for Se-containing composites. Differences in the Ni spectra of nickel sulfide, selenide, and telluride materials have been previously regarded as an indicator of the improved resistance to oxidation exhibited by the Se and Te materials.[7,25] Thus, an increase in metallic character with increasing Se incorporation for 10 and 25% composites not only agrees with the increasing quantity of NiSe visible in the XRD spectra but may also indicate that the composite material is more resistant to oxidation than the pure Ni_3S_2 electrocatalyst.

In agreement with the higher oxidation resistance of Se species, closer inspection of the Se 3d region for all composites (Figures 3d and S9d) shows that only a small degree of

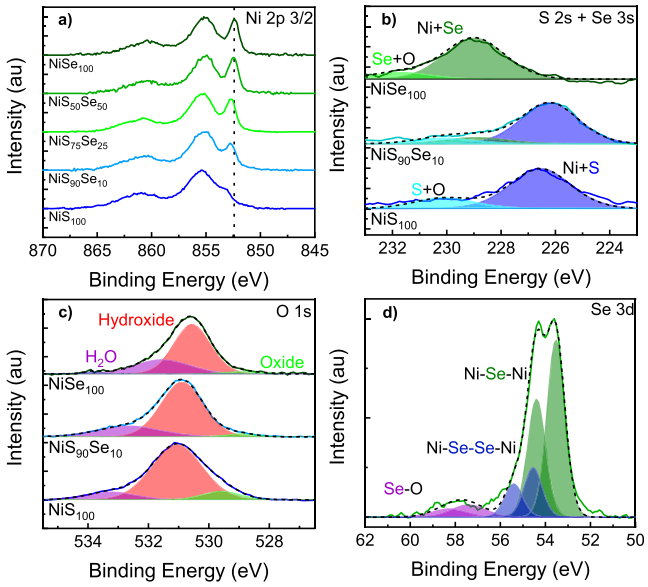

Figure 3. (a) Ni 2p 3/2 XPS spectra of all NiSSe composites, showing a gradual shift to lower binding energies with increasing Se content, indicating a more metallic character (b) XPS spectra of the S 2s and Se 3s regions for the NiS_{100}, $NiS_{90}Se_{10}$, and $NiSe_{100}$ samples. The addition of Se results in a decreased quantity of oxidized chalcogen at the surface. (c) O 1s XPS spectra for the NiS_{100}, $NiS_{90}Se_{10}$, and $NiSe_{100}$ composites, showing the contributions from surface hydroxides (red), oxides (green), and adsorbed water (purple). The addition of Se reduces the quantity of NiO_x species at the surface. (d) Se 3d spectra for the $NiS_{50}Se_{50}$ composite, showing contributions from single and dichalcogenide bonds and oxidized selenium species.

oxidized Se is present and that the predominant Se species present is typically assigned to nickel selenide compounds, with a 3d 5/2 peak at approximately 53 eV.[26] As previously noted by Cui and co-workers on Co chalcogenide OER catalysts, selenides and tellurides tend to be more resistant to oxidation than the corresponding sulfides.[27] Theoretical evidence of this can be observed when comparing Pourbaix diagrams for pure sulfide, selenide, and telluride materials (Figure S10).[28−30] In general, both Ni_3Se_2 and Ni_3Te_2 appear to be more stable than Ni_3S_2 across a wide range of pH value and potentials, although we do note that they are all expected to oxidize under OER conditions. Regardless, these data suggest that these materials possess a greater intrinsic stability, possibly because of the more metallic character of the material indicated by the Ni 2p region. In addition to the primary metal selenide peak, fitting of the spectrum reveals a second doublet of Se 3d peaks, however, with the 5/2 peak located at approximately 54.5 eV. This peak is more reduced than that of elemental Se[31] and therefore may instead be evidence of the surface presence of cubic $NiSe_2$, which exhibits a Se−Se bond.[32] Previous work has shown that the S 2p spectra of S-rich molybdenum sulfides likewise exhibit both a lower binding energy (BE) peak, representative of direct Mo−S−Mo bonds, and a higher BE peak, representative of Mo−S−S−Mo bonds.[33] The existence of $NiSe_2$ agrees well with the observed XPS spectra, and we can infer from the lack of associated peaks in XRD that this phase is likely in low abundance and may in fact only exist on the surface. Typically, the $NiSe_2$ phase accounted for approximately 20−25% of the total selenide species on the surface for all the Se-containing materials. As there does not appear to be any correlation between the

https://dx.doi.org/10.1021/acsami.0c00425
ACS Appl. Mater. Interfaces 2020, 12, 20366−20375

presence of $NiSe_2$ and improved OER performance, we do not think it plays a significant role in the observed differences in η_{10}.

Instead, OER performance is more closely related to the percentage of oxidized chalcogen present on the material surface prior to testing. By quantifying the amount of oxidized S and Se species in Figure S9b and then comparing this percentage to the η_{10} for each sample, we find similar changes in both the overpotential and the extent of surface oxidation as the level of Se incorporation changes (Figure S11). Both the Ni_3S_2-rich and the NiSe-rich composites show a clear decrease in η_{10} with decreasing S−O and Se−O species, and given that a material's surface species either contribute directly to the OER catalytic processes or indirectly influence the formation of other active sites and the overall electrical conductivity of the material, small changes in initial surface chemistry of an electrocatalyst can have significant impact on its OER performance. Previous work on a series of Ni−Se compounds showed that a previously oxidized NiO catalyst performed worse than a fresh NiSe catalyst which was oxidized during testing,[34] and other studies have shown that the type of oxidized surface species can play a large role in catalytic performance. For example, our group has previously shown that nickel sulfide catalysts fully oxidized to an amorphous hydroxide exhibited better OER performance than initially oxidized materials,[35] and Cui and co-workers showed similar results on a series of Co-based chalcogenides.[36] Thus, we hypothesize that in agreement with prior studies demonstrating the stability of Se compounds toward oxidation,[25] the introduction of Se into the Ni_3S_2 lattice mitigates oxidation of the surface prior to testing and may induce lattice strain (evidenced in Figure 1b) which creates more active sites for the OER. Although S incorporation into NiSe particles may also induce this defect/nucleation site effect, the presence of an excess of S (with its inherently lower resistance to oxidation) may result in more adverse surface oxidation on these composites even prior to catalysis. Furthermore, our particles are much larger than those of Wang *et al.*,[15] and thus, lattice defects may have less of an overall effect on the OER than surface oxidation for the larger $NiS_{50}Se_{50}$ particles.

3.4. Transmission Electron Microscopy. To study this oxidation behavior with much higher resolution, we used HRTEM and EDX mapping to examine catalyst oxidation before and after OER testing. To prepare materials for this comparison, chronopotentiometric stability experiments were performed on both composites, with the results reported in Figure 2b. Electrode stability was tested at a current density of 10 mA/cm^2, and initially, both the NiS_{100} and $NiS_{90}Se_{10}$ composites exhibited similar overpotentials near 375 mV. As the experiment progressed, however, the overpotential for the NiS_{100} sample increased by approximately 20% over 10 h, while the $NiS_{90}Se_{10}$ electrocatalyst did not exhibit any notable increase. The samples were run until failure, and the NiS_{100} sample failed after approximately 11 h, while the $NiS_{90}Se_{10}$ sample failed after approximately 22 h (Figure S12). This result agrees with our hypothesis regarding the stabilizing effect of the incorporated Se and is comparable to previously reported stabilities from Zeng *et al.* in the neutral electrolyte.[24] Following testing, the electrocatalysts were removed from the GC electrode *via* sonication and studied using HRTEM.

HRTEM analysis of the NiS_{100} material prior to testing shows that the micron-scale particles observed in the SEM images (Figure S1a) are agglomerates of crystalline particles roughly 50 nm in diameter (Figure S13), with additional crystalline particles less than 10 nm in diameter (Figure S14). Fast Fourier transform (FFT) analysis of the HRTEM images shows that the crystalline interior of the particles is composed of a mixture of NiS and Ni_3S_2 (Figure S14), in agreement with the XRD spectrum. Of note, the HRTEM shows the presence of a sub-10 nm layer of mostly amorphous materials surrounding the particle, which EDX mapping confirms to be O-rich (Figure S14b). This O-rich region also corresponds to the NiO species found in HRTEM, which indicates that the NiS_{100} catalyst exhibits both crystalline and amorphous oxide formation prior to OER testing; such oxidation corresponds to the hydroxide and oxide peaks observed in the O 1s XPS spectrum of the material. In contrast, HRTEM images of the as-synthesized $NiS_{90}Se_{10}$ (Figure S15a) show a much thinner amorphous layer on the imaged particles (Figure S15c). Lattice measurements show that these particles are composed primarily of NiS, Ni_3S_2, and NiSe phases, with evidence of NiOOH in the particle at spot 1, without any clear indication of NiO; this is in agreement with the previously discussed XPS results (Figure 2b). Similarly, the lower degree of oxidation visible in the EDX map of the composite (Figure S15b) indicates a diffuse amount of O in the material that, while most visible at the edges of the particles, is not as concentrated as in the NiS_{100} composite. Overall, these data support our hypothesis regarding the increased resistance to oxidation exhibited by the NiS_xSe_y composite materials.

After stability testing, both NiS_{100} and $NiS_{90}Se_{10}$ materials showed the formation of a clearly oxidized shell of the material surrounding an unoxidized core (Figure 4b,d), while also maintaining a homogeneous distribution of Ni, S, and Se in the unoxidized regions (Figures S16 and S17). Such behavior has been previously observed in other Ni sulfide-based electrocatalysts, with both amorphous and crystalline metal (oxy)-hydroxides observed as surface products.[35,37] Although the oxidized layer in the tested NiS_{100} sample shows particles with clearly visible crystal lattices (Figure 4c), the surface of the tested $NiS_{90}Se_{10}$ sample appears to be much more disordered (Figure 4e). Similarly, the thickness of the resulting oxide layer appears to differ with Se incorporation. From EDX mapping, the depth of the oxidized layer on the NiS_{100} sample appears to have doubled with OER testing, from ∼10 nm to approximately 20 nm over 10 h of testing. The $NiS_{90}Se_{10}$ sample also experiences growth, but only from 1−2 to 10 nm and over a much longer exposure of roughly 20 h. Comparing the two samples, the slower rate of oxidation exhibited by the $NiS_{90}Se_{10}$ sample appears to be further evidence of the stabilizing effect of Se incorporation.

The formation of an apparent core−shell particle after OER testing is interesting as there is significant evidence to suggest that metal chalcogenides, and sulfides in particular, are inherently unstable under alkaline OER reaction conditions.[5,27,35] Frequently, post-OER analysis shows that these materials are completely oxidized after testing,[35] although it appears as though the deliberate incorporation of metals such as Fe or Co may inhibit this[6]; we believe that the Se in our materials may be inducing a similar effect. Additionally, many previous reports on nickel sulfides explored NiS and NiS_2 compounds rather than the Ni_3S_2 material present here. Work from Nath and co-workers has shown that both Ni_3Te_2 and Ni_3Se_2 possess superior oxidative stability when compared to other telluride and selenide phases;[7,25] thus, it is possible that Ni_3S_2 may likewise possess increased stability toward surface

https://dx.doi.org/10.1021/acsami.0c00425
ACS Appl. Mater. Interfaces 2020, 12, 20366−20375

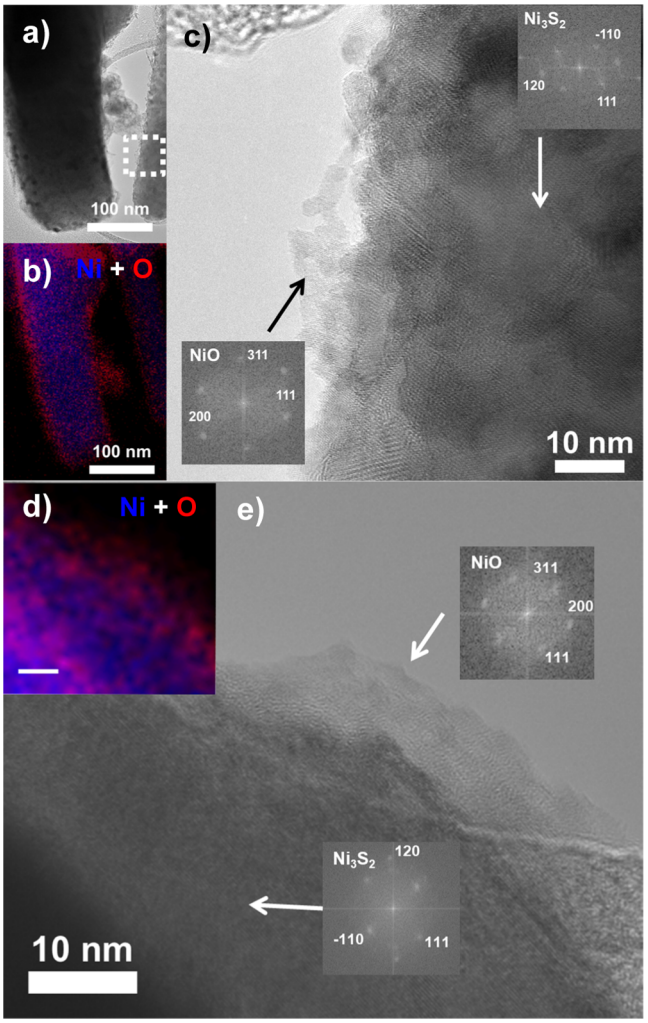

Figure 4. TEM image of post-OER NiS_{100} (a) with accompanying EDX mapping (b), showing the formation of an oxidized shell approximately 20 nm thick surrounding an unoxidized interior. HRTEM shows that the oxidized region appears relatively crystalline and is composed of NiO, while the interior is composed of Ni_3S_2. EDX mapping of the $NiS_{90}Se_{10}$ material [(d), scale bar 10 nm] shows a similarly oxidized surface, which is much thinner (10 nm) with HRTEM and FFT (e) likewise corresponding to NiO at the surface and Ni_3S_2 in the bulk. This oxide appears less particulate than the NiS_{100} material, however.

oxidation as compared to NiS or NiS_2 even before the addition of Se. Therefore, we suggest that the minimal oxidation of $NiS_{90}Se_{10}$ observed after long-term testing is a result of enhanced oxidative resistance due to both Se incorporation and this Ni_3S_2 phase. Regarding performance and stability, Se incorporation likely induces the formation of a more defective, active amorphous oxidized layer at the surface and increases the conductivity of the material as compared to a Se-free material. The increased conductivity of the material may also help explain the improved stability of the $NiS_{90}Se_{10}$ material. Because of the increased conductivity and OER performance of the electrocatalyst, less internal resistive loss occurs and lower overpotentials are required to drive the OER forward, reducing the likelihood of parasitic side reactions such as self-oxidation. Our measurements of Faradaic efficiency (Figure S5) show that NiS_{100} shows reduced efficiency for the OER at higher applied current densities (and larger overpotentials) when compared to the $NiS_{90}Se_{10}$, providing support for this hypothesis. In this way, the Se incorporation would increase the stability of the material by increasing conductivity, and thereby indirectly mitigate undesired reactions. Combined with the likely higher intrinsic stability of the Ni_3S_2 phase and the lattice defects in the particles, this could explain why $NiS_{90}Se_{10}$ shows the best performance of all materials studied here as it combines proper crystal phase, active lattice defects, and increased conductivity to improve electrocatalytic performance and minimize damage to the catalyst.

4. CONCLUSIONS

In summary, we have used a scalable hydrothermal synthesis to create a series of nickel sulfoselenide materials for use as OER electrocatalysts in alkaline solution. Through this method, we created composites consisting primarily of Se-modified Ni_3S_2 from precursor mixtures with low Se concentrations, while a S-modified NiSe phase became more abundant with increasing precursor Se concentration. The predominant products and the relative extents of Se or S incorporation were monitored by XRD, while interrogation by XPS and EDX confirmed that the desired overall S/Se ratio was achieved. SEM and HRTEM measurements revealed that the synthesized materials were micron-sized clusters of smaller nanocrystals, and Kr surface adsorption analysis determined that all of the materials possessed similar BET surface areas (<20 m^2/g). Surface chemistry analysis with XPS suggested that Se addition appeared to reduce the extent of oxidation in the composites, resulting in more hydroxide than oxide species on the surface. OER overpotential measurements showed that Se-modified Ni_3S_2 possessed superior catalytic ability and stability when compared to the other composites, with $NiS_{90}Se_{10}$ having an η_{10} of 318 mV and stable performance over 20 h. Improvement in electrocatalytic performance was correlated to a decrease in the amount of oxidized S or Se (determined *via* XPS), leading us to conclude that Se incorporation may promote the formation of lattice defects that lead to fewer but more active initial (oxy)hydroxide species, which in turn act as the true OER electrocatalyst material. Furthermore, EIS spectra show that Se incorporation leads to a more conductive material, and this increase in conductivity may also improve electrocatalytic performance and stability by reducing the overpotential needed to perform the OER and thus reduce undesired side reactions such as self-oxidation, as supported by Faradaic efficiency measurements. This is further supported by HRTEM and EDX analyses, which show clear differences in the type and extent of oxidized products that form on NiS_{100} and $NiS_{90}Se_{10}$ electrocatalysts before and after long-term OER testing, indicating a lower extent of oxidation in Se-containing Ni_3S_2 materials. Together, our results suggest that mixed chalcogenides represent an exciting new class of OER precatalysts where differences in chalcogen composition can impact the physicochemical and electrochemical properties of both the as-synthesized metal chalcogenide and the final electrocatalytically active metal (oxy)hydroxide. Further exploration of these exciting materials to better understand their structure–property–performance relationships should allow for rational engineering of efficient earth-abundant Ni electrocatalysts with enhanced performance and stability. With lower associated material and operating costs, widespread implementation of renewably powered water electrolysis technologies could become a viable solution for sustainable hydrogen production for carbon-free fuels and industrial feedstocks.

https://dx.doi.org/10.1021/acsami.0c00425
ACS Appl. Mater. Interfaces 2020, 12, 20366–20375

■ ASSOCIATED CONTENT

Supporting Information

The Supporting Information is available free of charge at https://pubs.acs.org/doi/10.1021/acsami.0c00425.

SEM images of all catalysts, Kr-adsorption and BET surface area plots, mass activity measurements, EIS spectra, TXRF Ni and Se content quantification of the tested electrolyte solution, Faradaic efficiency measurements, BET-derived surface area CVs, additional XPS spectra and overpotential/surface oxidation comparison, long-term electrochemical testing results, additional TEM images, and EDX elemental mapping before and after testing (PDF)

■ AUTHOR INFORMATION

Corresponding Author

C. Buddie Mullins − *Department of Chemistry, McKetta Department of Chemical Engineering, and Texas Materials Institute, Center for Electrochemistry, University of Texas at Austin, Austin 78712, Texas, United States;* orcid.org/0000-0003-1030-4801; Email: mullins@che.utexas.edu

Authors

Bryan R. Wygant − *Department of Chemistry, University of Texas at Austin, Austin 78712, Texas, United States*

Anna H. Poterek − *Department of Civil, Architectural, and Environmental Engineering, University of Texas at Austin, Austin 78712, Texas, United States*

James N. Burrow − *McKetta Department of Chemical Engineering, University of Texas at Austin, Austin 78712, Texas, United States*

Complete contact information is available at: https://pubs.acs.org/10.1021/acsami.0c00425

Notes

The authors declare no competing financial interest.

■ ACKNOWLEDGMENTS

The authors gratefully acknowledge the support of the Robert A. Welch Foundation *via* grant F-1436 and the National Science Foundation *via* grant no. CHE-1664941 and also grant no. 0618242 for funding the X-ray photoelectron spectrometer used in this work. The authors also thank the lab of Dr. Richard Crooks and Dr. Yi Peng for assistance with the RRDE experiments in this work and the lab of Dr. Victor Hugo Ramos Sánchez for assistance with TXRF quantification.

■ REFERENCES

(1) Denholm, P.; O'Connell, M.; Brinkman, G.; Jorgenson, J. *Overgeneration from Solar Energy in California: A Field Guide to the Duck Chart* (NREL/TP-6A20-65023). Technical Report; National Renewable Energy Lab, 2015; No. November, p 46.

(2) You, B.; Sun, Y. Innovative Strategies for Electrocatalytic Water Splitting. *Acc. Chem. Res.* **2018**, *51*, 1571−1580.

(3) Gorlin, Y.; Jaramillo, T. F. A Bifunctional Nonprecious Metal Catalyst for Oxygen Reduction and Water Oxidation. *J. Am. Chem. Soc.* **2010**, *132*, 13612−13614.

(4) Batchellor, A. S.; Boettcher, S. W. Pulse-Electrodeposited Ni-Fe (Oxy)Hydroxide Oxygen Evolution Electrocatalysts with High Geometric and Intrinsic Activities at Large Mass Loadings. *ACS Catal.* **2015**, *5*, 6680−6689.

(5) Zhu, Y.; Chen, H.-C.; Hsu, C.-S.; Lin, T.-S.; Chang, C.-J.; Chang, S.-C.; Tsai, L.-D.; Chen, H. M. Operando Unraveling of the Structural and Chemical Stability of P-Substituted CoSe 2 Electrocatalysts toward Hydrogen and Oxygen Evolution Reactions in Alkaline Electrolyte. *ACS Energy Lett.* **2019**, *4*, 987−994.

(6) Zhou, M.; Weng, Q.; Zhang, X.; Wang, X.; Xue, Y.; Zeng, X.; Bando, Y.; Golberg, D. In Situ Electrochemical Formation of Core−Shell Nickel−Iron Disulfide and Oxyhydroxide Heterostructured Catalysts for a Stable Oxygen Evolution Reaction and the Associated Mechanisms. *J. Mater. Chem. A* **2017**, *5*, 4335−4342.

(7) De Silva, U.; Masud, J.; Zhang, N.; Hong, Y.; Liyanage, W. P. R.; Asle Zaeem, M.; Nath, M. Nickel Telluride as a Bifunctional Electrocatalyst for Efficient Water Splitting in Alkaline Medium. *J. Mater. Chem. A* **2018**, *6*, 7608−7622.

(8) Zhang, J.-Y.; Lv, L.; Tian, Y.; Li, Z.; Ao, X.; Lan, Y.; Jiang, J.; Wang, C. Rational Design of Cobalt-Iron Selenides for Highly Efficient Electrochemical Water Oxidation. *ACS Appl. Mater. Interfaces* **2017**, *9*, 33833−33840.

(9) Jiang, N.; Tang, Q.; Sheng, M.; You, B.; Jiang, D.-e.; Sun, Y. Nickel Sulfides for Electrocatalytic Hydrogen Evolution under Alkaline Conditions: A Case Study of Crystalline NiS, NiS 2, and Ni 3 S 2 Nanoparticles. *Catal. Sci. Technol.* **2016**, *6*, 1077−1084.

(10) Yu, J.; Cheng, G.; Luo, W. Ternary Nickel-Iron Sulfide Microflowers as a Robust Electrocatalyst for Bifunctional Water Splitting. *J. Mater. Chem. A* **2017**, *5*, 15838−15844.

(11) Du, X.; Ma, G.; Zhang, X. Experimental and Theoretical Understanding on Electrochemical Activation Processes of Nickel Selenide for Excellent Water-Splitting Performance: Comparing the Electrochemical Performances with M-NiSe (M = Co, Cu, and V). *ACS Sustainable Chem. Eng.* **2019**, *7*, 19257−19267.

(12) Du, X.; Su, H.; Zhang, X. Metal-Organic Framework-Derived Cu-Doped Co9S8 Nanorod Array with Less Low-Valence Co Sites as Highly Efficient Bifunctional Electrodes for Overall Water Splitting. *ACS Sustainable Chem. Eng.* **2019**, *7*, 16917−16926.

(13) Jin, S. Are Metal Chalcogenides, Nitrides, and Phosphides Oxygen Evolution Catalysts or Bifunctional Catalysts? *ACS Energy Lett.* **2017**, *2*, 1937−1938.

(14) Wygant, B. R.; Kawashima, K.; Mullins, C. B. Catalyst or Precatalyst? The Effect of Oxidation on Transition Metal Carbide, Pnictide, and Chalcogenide Oxygen Evolution Catalysts. *ACS Energy Lett.* **2018**, *3*, 2956−2966.

(15) Wang, M.; Dang, Z.; Prato, M.; Shinde, D. V.; De Trizio, L.; Manna, L. Ni−Co−S−Se Alloy Nanocrystals: Influence of the Composition on Their in Situ Transformation and Electrocatalytic Activity for the Oxygen Evolution Reaction. *ACS Appl. Nano Mater.* **2018**, *1*, 5753−5762.

(16) Hu, C.; Zhang, L.; Zhao, Z.-J.; Li, A.; Chang, X.; Gong, J. Synergism of Geometric Construction and Electronic Regulation: 3D Se-(NiCo)S x /(OH) x Nanosheets for Highly Efficient Overall Water Splitting. *Adv. Mater.* **2018**, *30*, 1705538.

(17) Zhang, J.; Li, Y.; Zhu, T.; Wang, Y.; Cui, J.; Wu, J.; Xu, H.; Shu, X.; Qin, Y.; Zheng, H.; Ajayan, P. M.; Zhang, Y.; Wu, Y. 3D Coral-Like Ni3S2 on Ni Foam as a Bifunctional Electrocatalyst for Overall Water Splitting. *ACS Appl. Mater. Interfaces* **2018**, *10*, 31330−31339.

(18) Khan, N. A.; Rashid, N.; Junaid, M.; Zafar, M. N.; Faheem, M.; Ahmad, I. NiO/NiS Heterostructures: An Efficient and Stable Electrocatalyst for Oxygen Evolution Reaction. *ACS Appl. Energy Mater.* **2019**, *2*, 3587−3594.

(19) Zhou, W.; Wu, X.-J.; Cao, X.; Huang, X.; Tan, C.; Tian, J.; Liu, H.; Wang, J.; Zhang, H. Ni3S2 Nanorods/Ni Foam Composite Electrode with Low Overpotential for Electrocatalytic Oxygen Evolution. *Energy Environ. Sci.* **2013**, *6*, 2921−2924.

(20) Zhu, W.; Yue, X.; Zhang, W.; Yu, S.; Zhang, Y.; Wang, J.; Wang, J. Nickel Sulfide Microsphere Film on Ni Foam as an Efficient Bifunctional Electrocatalyst for Overall Water Splitting. *Chem. Commun.* **2016**, *52*, 1486−1489.

(21) Shannon, R. D. Revised Effective Ionic Radii and Systematic Studies of Interatomic Distances in Halides and Chalcogenides. *Acta Crystallogr., Sect. A: Cryst. Phys., Diffr., Theor. Gen. Crystallogr.* **1976**, *32*, 751−767.

(22) Tang, C.; Cheng, N.; Pu, Z.; Xing, W.; Sun, X. NiSe Nanowire Film Supported on Nickel Foam: An Efficient and Stable 3D Bifunctional Electrode for Full Water Splitting. *Angew. Chem., Int. Ed.* **2015**, *54*, 9351−9355.
(23) McCrory, C. C. L.; Jung, S.; Peters, J. C.; Jaramillo, T. F. Benchmarking Heterogeneous Electrocatalysts for the Oxygen Evolution Reaction. *J. Am. Chem. Soc.* **2013**, *135*, 16977−16987.
(24) Zeng, L.; Sun, K.; Chen, Y.; Liu, Z.; Chen, Y.; Pan, Y.; Zhao, R.; Liu, Y.; Liu, C. Neutral-PH Overall Water Splitting Catalyzed Efficiently by a Hollow and Porous Structured Ternary Nickel Sulfoselenide Electrocatalyst. *J. Mater. Chem. A* **2019**, *7*, 16793−16802.
(25) Swesi, A. T.; Masud, J.; Nath, M. Nickel Selenide as a High-Efficiency Catalyst for Oxygen Evolution Reaction. *Energy Environ. Sci.* **2016**, *9*, 1771−1782.
(26) Mandale, A. B.; Badrinarayanan, S.; Date, S. K.; Sinha, A. P. B. Photoelectron-Spectroscopic Study of Nickel, Manganese and Cobalt Selenides. *J. Electron Spectrosc. Relat. Phenom.* **1984**, *33*, 61−72.
(27) Chen, W.; Liu, Y.; Li, Y.; Sun, J.; Qiu, Y.; Liu, C.; Zhou, G.; Cui, Y. In Situ Electrochemically Derived Nanoporous Oxides from Transition Metal Dichalcogenides for Active Oxygen Evolution Catalysts. *Nano Lett.* **2016**, *16*, 7588−7596.
(28) Persson, K. A.; Waldwick, B.; Lazic, P.; Ceder, G. Prediction of Solid-Aqueous Equilibria: Scheme to Combine First-Principles Calculations of Solids with Experimental Aqueous States. *Phys. Rev. B: Condens. Matter Mater. Phys.* **2012**, *85*, 235438.
(29) Jain, A.; Ong, S. P.; Hautier, G.; Chen, W.; Richards, W. D.; Dacek, S.; Cholia, S.; Gunter, D.; Skinner, D.; Ceder, G.; Persson, K. A. Commentary: The Materials Project: A Materials Genome Approach to Accelerating Materials Innovation. *APL Mater.* **2013**, *1*, 011002.
(30) Singh, A. K.; Zhou, L.; Shinde, A.; Suram, S. K.; Montoya, J. H.; Winston, D.; Gregoire, J. M.; Persson, K. A. Electrochemical Stability of Metastable Materials. *Chem. Mater.* **2017**, *29*, 10159−10167.
(31) Moulder, J. F.; Stickle, W. F.; Sobol, P. E.; Bomben, K. D. *Handbook of X-Ray Photoelectron Spectroscopy*; Perkin-Elmer Corporation, 1979; Vol. 3.
(32) Fan, H.; Zhang, M.; Zhang, X.; Qian, Y. Hydrothermal Growth of NiSe 2 Tubular Microcrystals Assisted by PVA. *J. Cryst. Growth* **2009**, *311*, 4530−4534.
(33) Mabayoje, O.; Liu, Y.; Wang, M.; Shoola, A.; Ebrahim, A. M.; Frenkel, A. I.; Mullins, C. B. Electrodeposition of MoS x Hydrogen Evolution Catalysts from Sulfur-Rich Precursors. *ACS Appl. Mater. Interfaces* **2019**, *11*, 32879−32886.
(34) Xu, K.; Ding, H.; Lv, H.; Tao, S.; Chen, P.; Wu, X.; Chu, W.; Wu, C.; Xie, Y. Understanding Structure-Dependent Catalytic Performance of Nickel Selenides for Electrochemical Water Oxidation. *ACS Catal.* **2017**, *7*, 310−315.
(35) Mabayoje, O.; Shoola, A.; Wygant, B. R.; Mullins, C. B. The Role of Anions in Metal Chalcogenide Oxygen Evolution Catalysis: Electrodeposited Thin Films of Nickel Sulfide as "Pre-Catalysts". *ACS Energy Lett.* **2016**, *1*, 195−201.
(36) Chen, W.; Wang, H.; Li, Y.; Liu, Y.; Sun, J.; Lee, S.; Lee, J.-S.; Cui, Y. In Situ Electrochemical Oxidation Tuning of Transition Metal Disulfides to Oxides for Enhanced Water Oxidation. *ACS Cent. Sci.* **2015**, *1*, 244.
(37) Xu, X.; Song, F.; Hu, X. A Nickel Iron Diselenide-Derived Efficient Oxygen-Evolution Catalyst. *Nat. Commun.* **2016**, *7*, 12324.

https://dx.doi.org/10.1021/acsami.0c00425
ACS Appl. Mater. Interfaces 2020, 12, 20366−20375